



Figures and figure supplements

Dlk1-Dio3 locus-derived lncRNAs perpetuate postmitotic motor neuron cell fate and subtype identity

Ya-Ping Yen et al

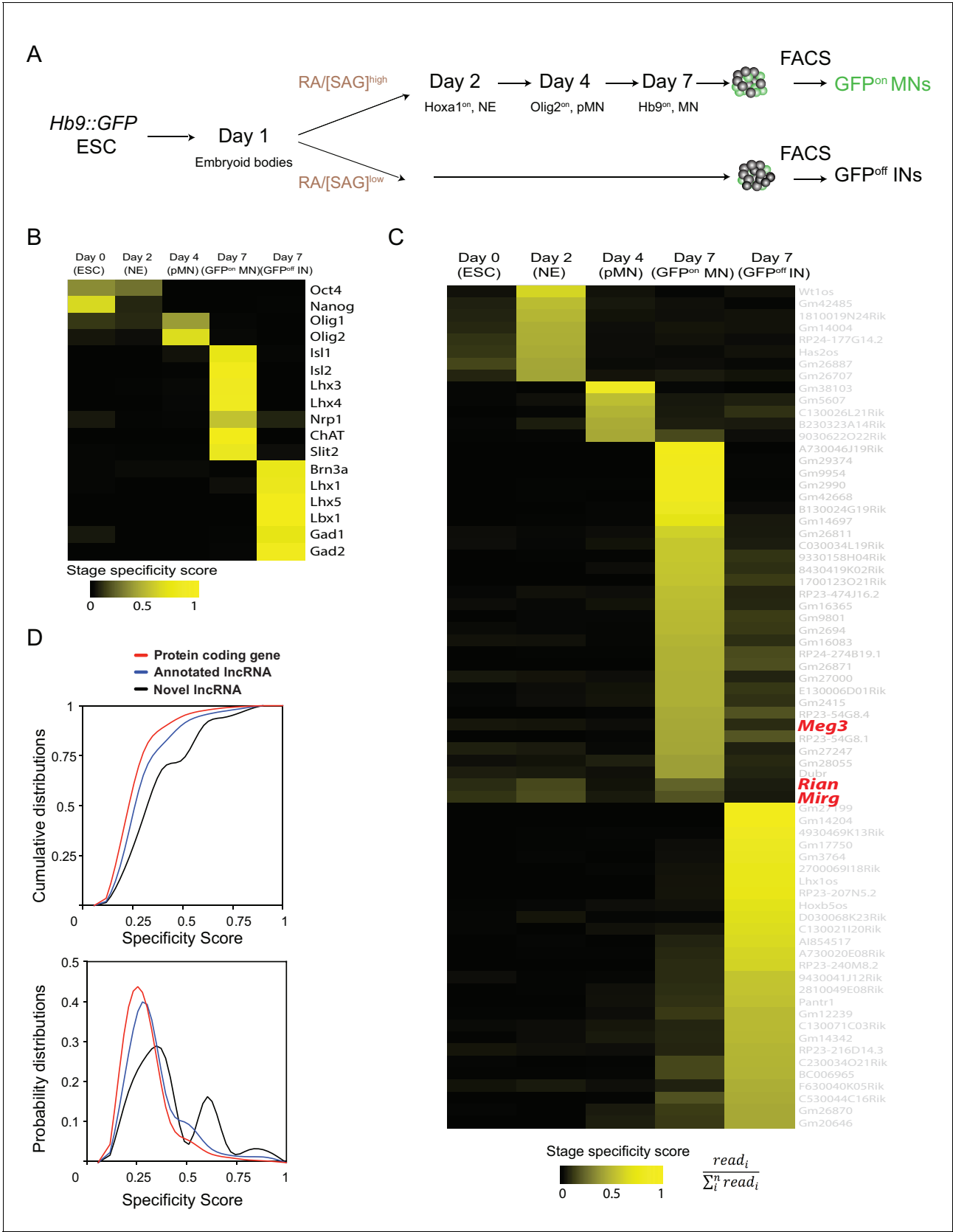


Figure 1. Identification of cell-type-specific lncRNAs during motor neuron differentiation. (A) Schematic illustration of the differentiation process from *Hb9::GFP* ESCs to spinal MNs. RA: retinoic acid. SAG: Smoothed agonist. ESC: embryonic stem cell. NE: neural epithelium. pMN: motor neuron

Figure 1 continued on next page

Figure 1 continued

progenitor. MN: motor neuron. IN: interneuron. **(B and C)** Heatmaps presenting the abundances of known cell transcription factors **(B)** and the abundances of lncRNA signatures **(C)** across each stage from ESCs to postmitotic MNs and INs (color indicates specificity scores). **(D)** Cumulative distributions (above) and probability distributions (below) of the stage specificity score of different categories of genes (protein coding genes [red], annotated lncRNAs [blue] and novel lncRNAs [black]), representing a measure of differential expression for each transcript across the cell types. The distribution reveals that annotated lncRNAs and novel lncRNAs manifest significantly higher specificity (according to Kolmogorov-Smirnov tests) than protein-coding genes.

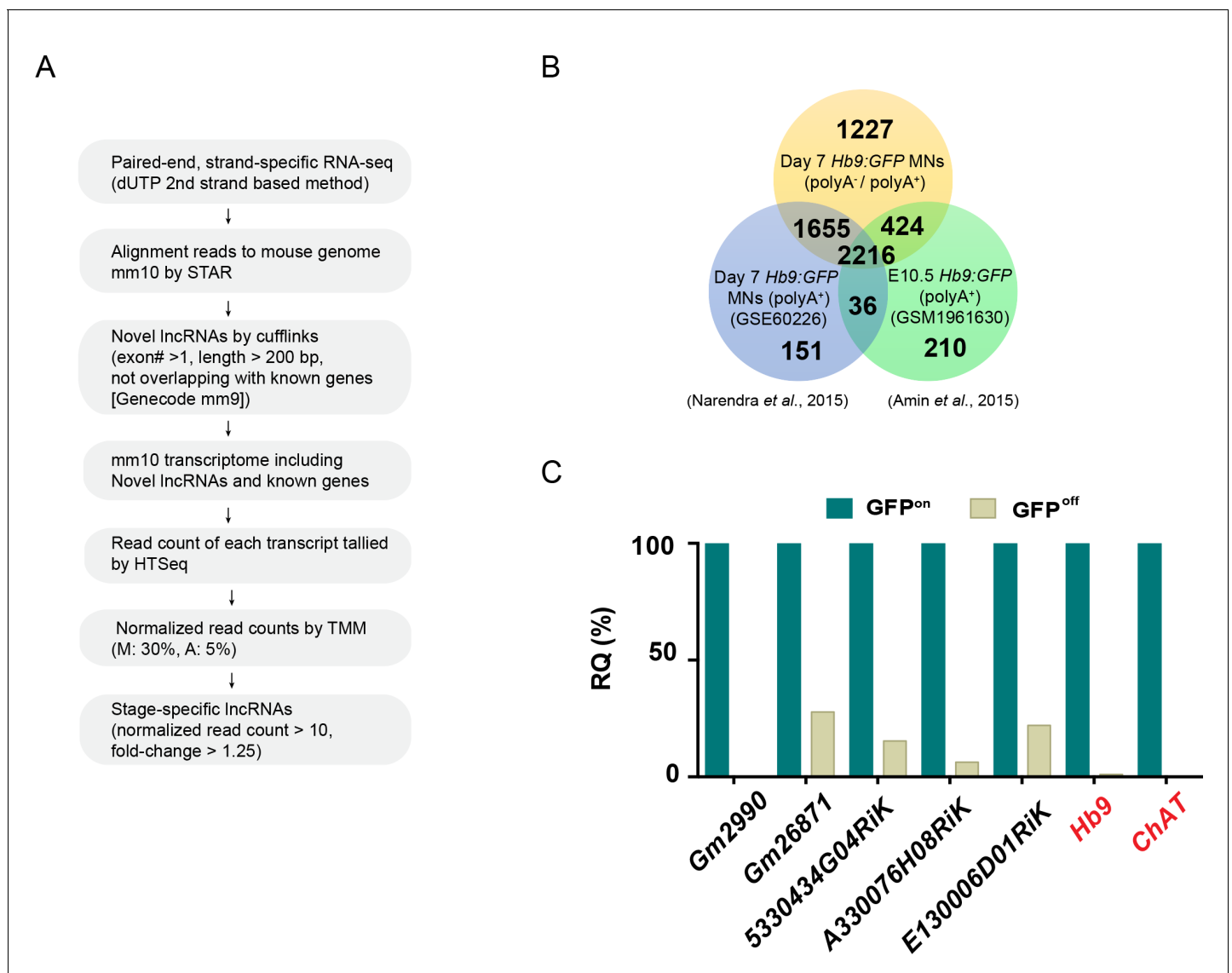


Figure 1—figure supplement 1. Systematic identification and verification of motor neuron signature lncRNAs. (A) Workflow of the RNA-seq analysis to identify cell-type-enriched lncRNAs. (B) The strand-specific RNA-seq performed in this study (orange) identified many more lncRNAs compared to previously published studies (blue and green) that used polyA⁺ selection RNA-seq. (C) Identified MN-signature lncRNAs were verified by qPCR from FACS-sorted GFP^{on} MNs, whereas GFP^{off} INs were used to reflect their specificity and relative quantity (RQ). *Hb9* and *ChAT* are mature MN markers.

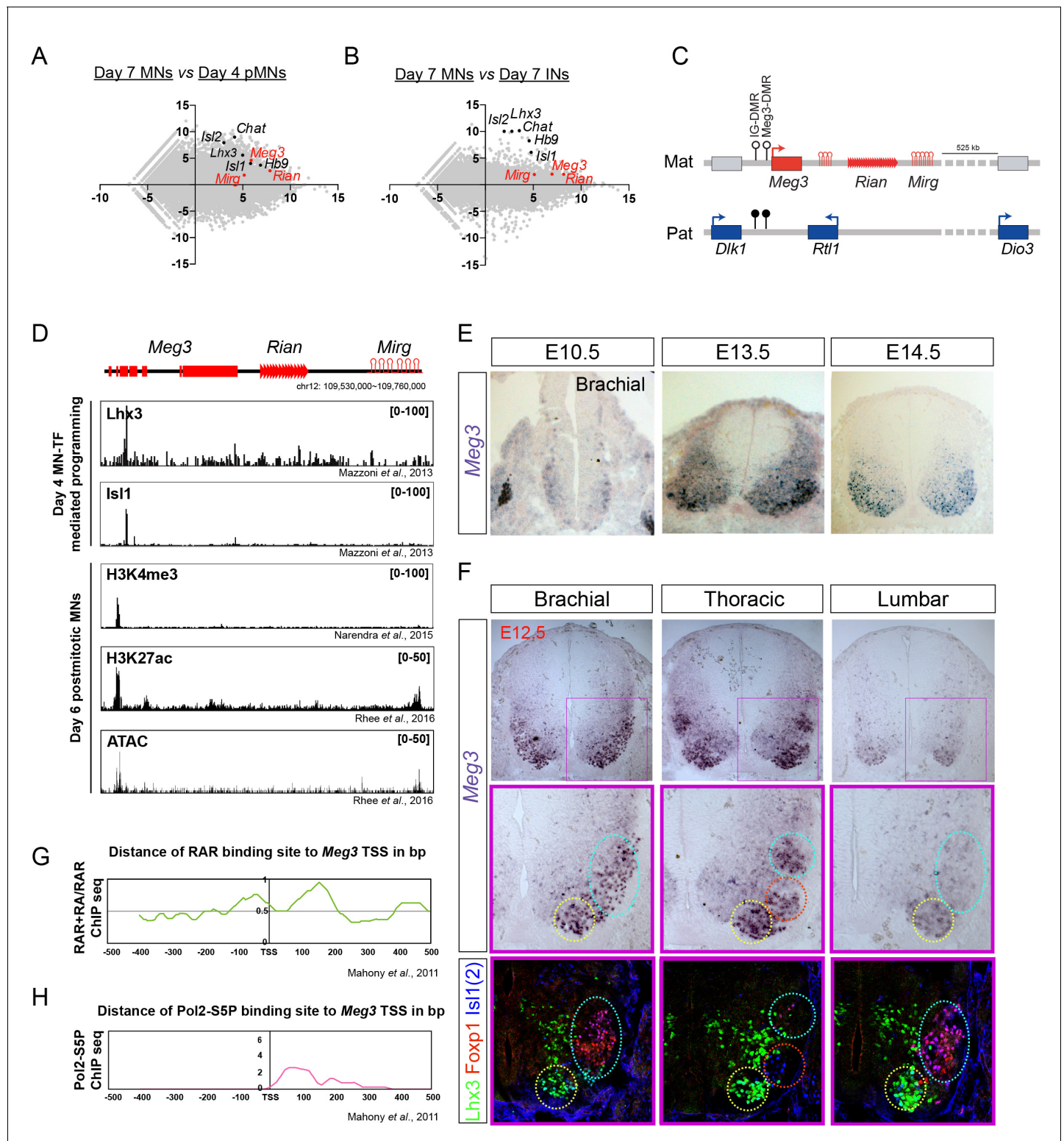


Figure 2. *Dlk1-Dio3* locus-derived lncRNAs are enriched in postmitotic motor neurons. (A and B) MA plots demonstrate that *Meg3*, *Rian*, and *Mirg* are postmitotic (day 7 MNs vs. day 4 pMN; A) MN signature (day 7 MNs vs. day 7 INs; B) lncRNAs. X-axis: mean abundance; Y-axis: log₂ fold-change. (C) Illustration of the imprinted *Dlk1-Dio3* locus. The lncRNAs of the maternally-inherited allele (in red) are on mouse chromosome 12. The miRNA and C/D snoRNA genes are shown by hairpin loops and triangles, respectively. (D) Comparison of ChIP-seq for MN transcription factors (Lhx3 and Isl1), H3K4me3, and H3K27ac, together with ATAC-seq of the *Dlk1-Dio3* locus. (E) In situ hybridization shows that *Meg3* is gradually enriched and restricted in postmitotic MNs in the developing spinal cord. (F) In situ hybridization together with adjacent sections of immunostaining on E12.5 segmental spinal cord

Figure 2 continued on next page

Figure 2 continued

cords demonstrate that *Meg3* is enriched at brachial and thoracic MNs (*Isl1/2^{on}*), but no preference for columnar MN subtypes was revealed for *Foxp1* or *Lhx3*. (**G and H**) RAR binding and recruitment of the elongating form of Pol2 to the *Meg3* transcription start site (TSS) occur within 8 hr of retinoic acid (RA) exposure.

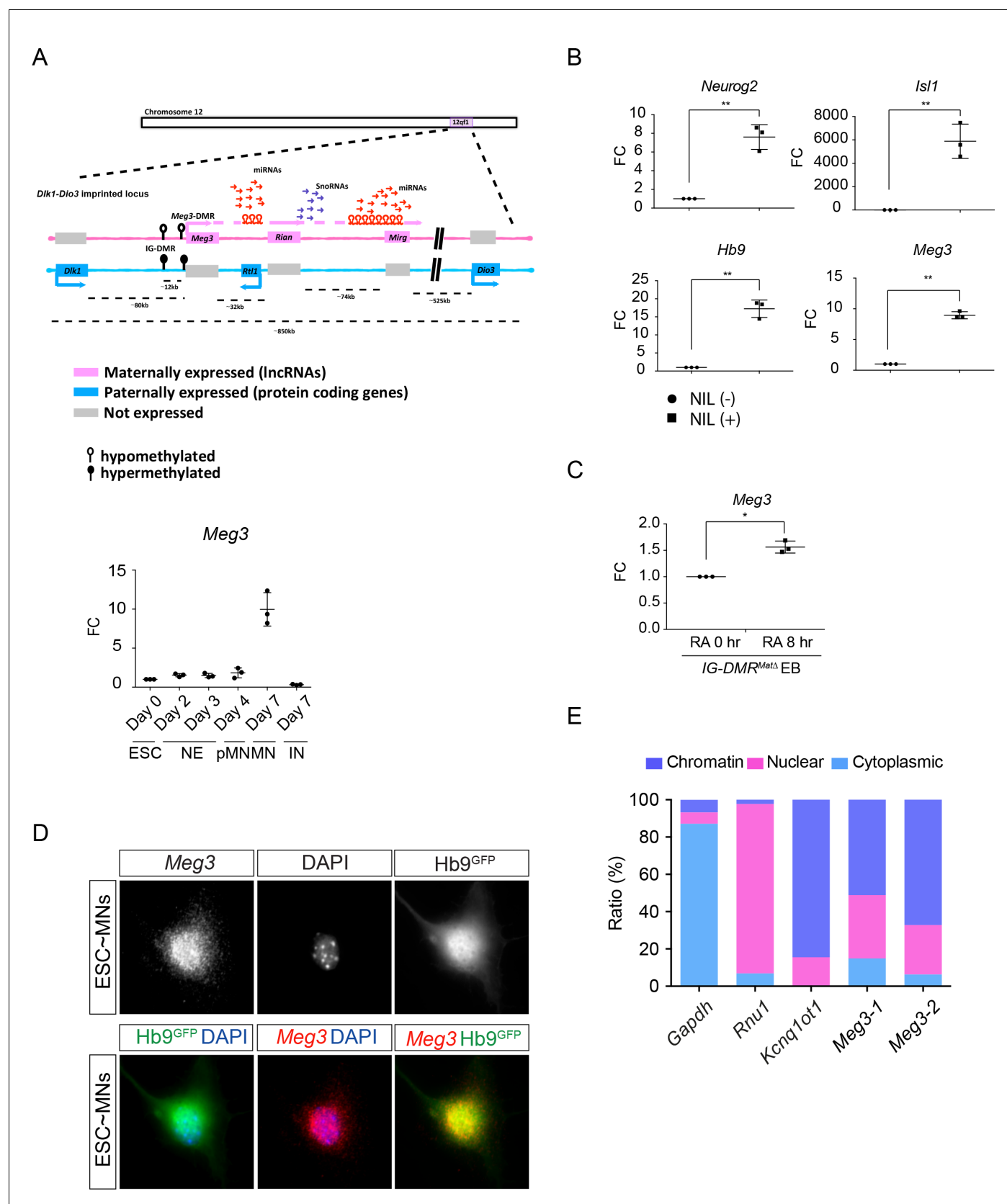


Figure 2—figure supplement 1. Characterization of the lncRNAs in the *Dlk1-Dio3* locus. (A) Illustration of the imprinted *Dlk1-Dio3* locus. The lncRNAs on the maternally-inherited allele (in pink) and protein-coding genes from the paternally-inherited allele (in blue) are depicted. miRNA genes are shown

Figure 2—figure supplement 1 continued on next page

Figure 2—figure supplement 1 continued

by hairpin loops. Arrows indicate the transcription directions. The *IG-DMR* site is hypomethylated (open circles) on the maternally-inherited allele, but hypermethylated (filled circles) on the paternally-inherited allele. Lower panel shows the qPCR analysis of *Meg3* expression in ESCs, NEs, pMNs, MNs and INs (n = 3 independent experiments; FC: fold-change). (**B and C**) qPCR reveals that MN transcription factors (*Neurog2-Isl1-Lhx3*), as long as adding RA, can induce *Meg3* expression in the *IG-DMR^{matΔ}* ESCs (FC: fold-change; error bars represent SD, n = 3, * p-value<0.05, ** p-value<0.01 by Student's t-test). (**D**) Panels show single molecule RNA FISH of *Meg3* in *Hb9::GFP* ESC-MNs. (**E**) Subcellular fractionation of ESC-MNs revealed that *Meg3* is not only enriched in the nuclei, but also highly chromatin-associated. Two independent *Meg3* primers were used. *Gapdh*, *Rnu1*, and *Kcnq1ot1* were used to reflect the purity of cytoplasmic, nuclear, and chromatin-associated fractions, respectively.

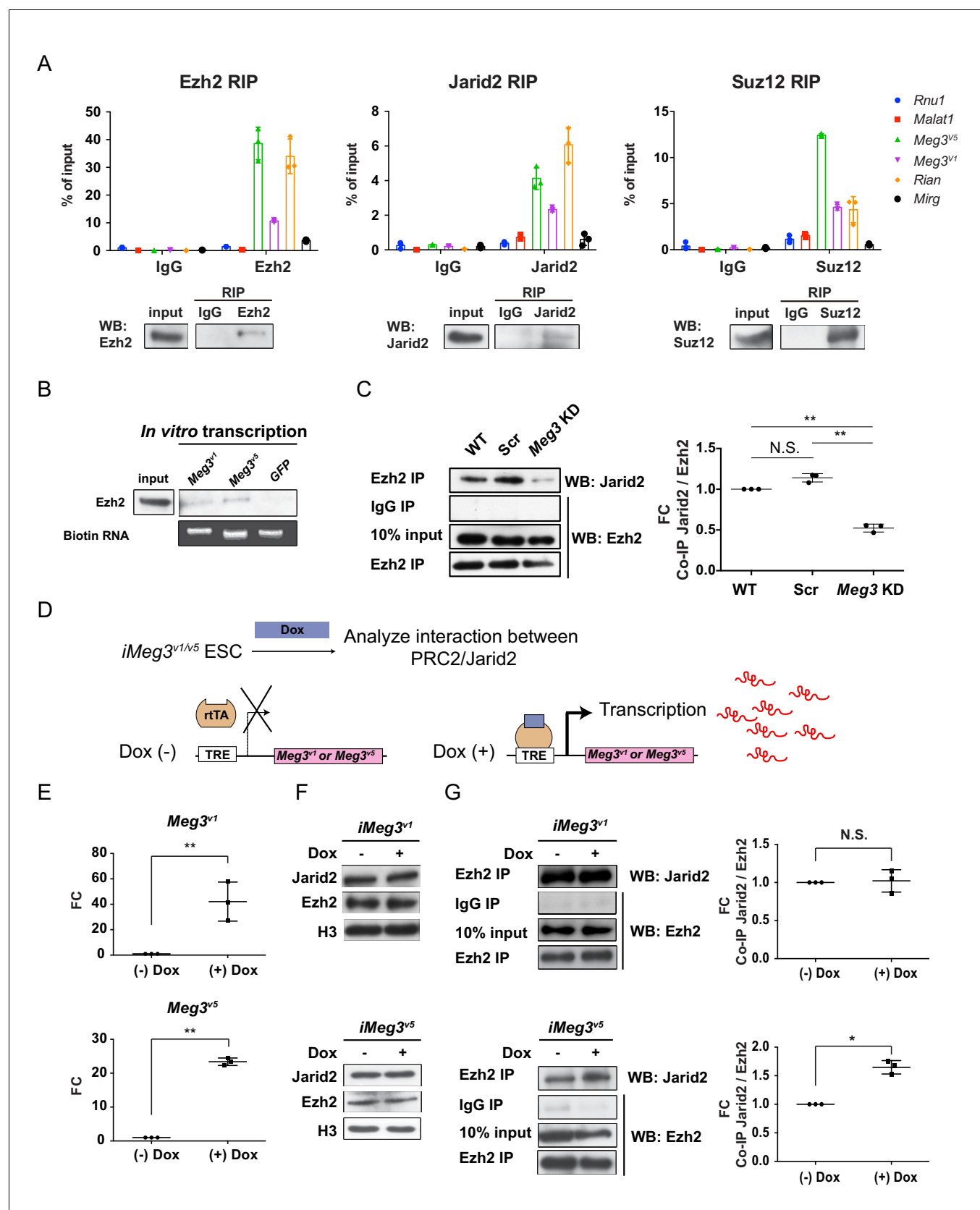


Figure 3. *Meg3* facilitates the non-stoichiometric interaction of the PRC2 complex and Jarid2. (A) Ezh2, Jarid2, and Suz12 immunoprecipitation specifically retrieves *Meg3* RNA isoforms (v1 and v5). *Rnu1* RNA and *Malat1* lncRNA are negative controls. 10% input was used to normalize the

Figure 3 continued on next page

Figure 3 continued

retrieval efficiency (error bars represent SD, $n = 3$ independent experiments). Immunoblotting reflects the recovery of Ezh2, Jarid2 and Suz12 proteins using the corresponding antibodies. (B) In vitro-transcribed, biotinylated *Meg3* RNA isoforms retrieved Ezh2. (C) Ezh2 interacts with Jarid2 in ESC-MNs, but knockdown of *Meg3* impairs this interaction. The abundance of Jarid2 is shown on the right (N.S.: not significant; error bars represent SD, $n = 3$ independent experiments; ** p -value <0.01 by Student's t -test). (D and E) The design of inducible 'Tet-On' ESC lines expressing *Meg3^{v1}* or *Meg3^{v5}* under the doxycycline (Dox)-regulated promoter. In the presence of Dox, the reverse tetracycline-controlled transactivator (rtTA) is recruited to the TRE (tetracycline response element), thereby initiating robust transcription of *Meg3^{v1}* or *Meg3^{v5}*, respectively. (F) Overexpression of *Meg3^{v1}* or *Meg3^{v5}* does not alter the protein levels of Ezh2 or Jarid2. (G) *Meg3^{v5}* but not *Meg3^{v1}* stimulates more Ezh2 and Jarid2 interaction. The abundances of Jarid2 are shown on the right (FC: fold-change; N.S.: not significant; error bars represent SD, $n = 3$ independent experiments; * p -value <0.05 , ** p -value <0.01 by Student's t -test).

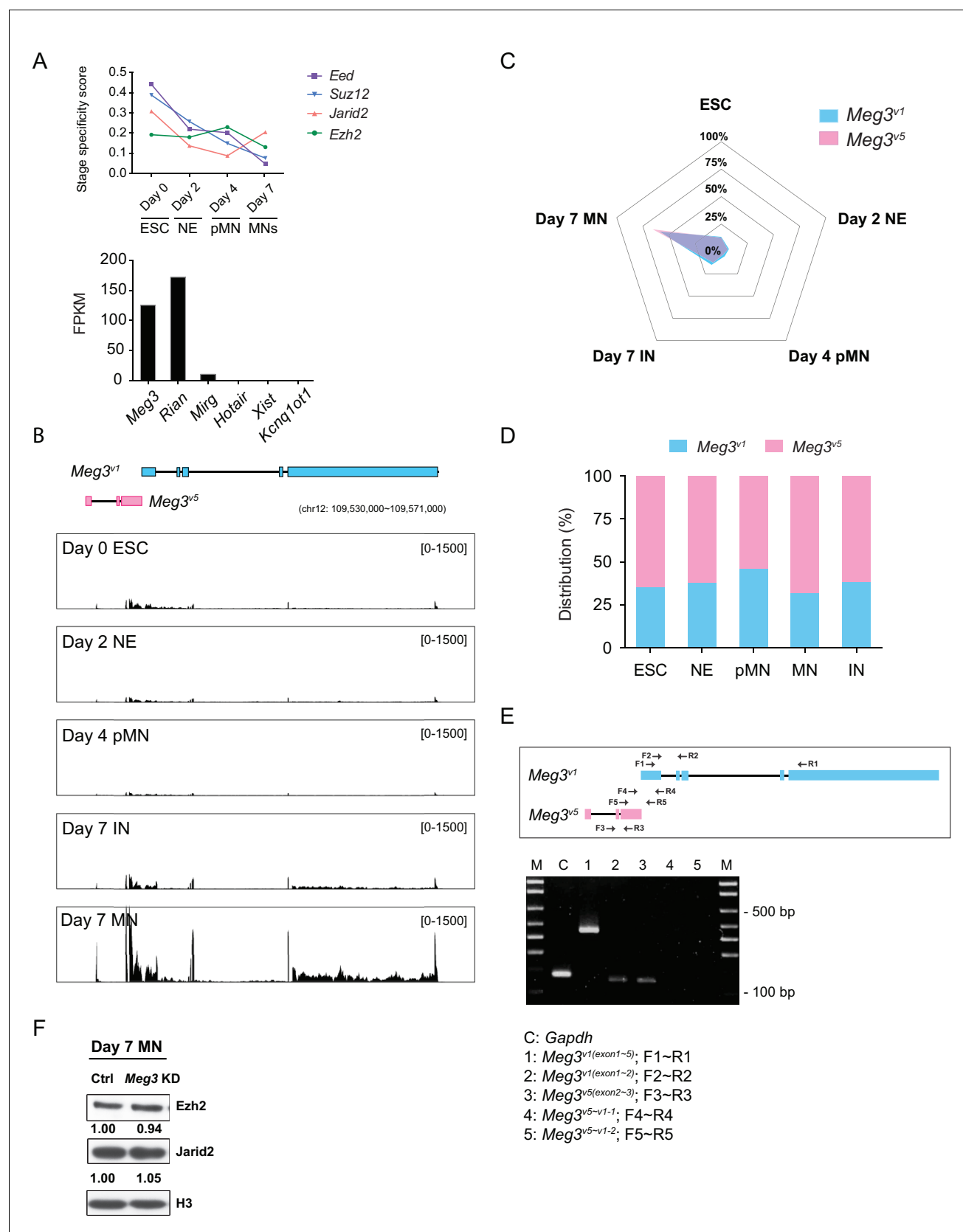


Figure 3—figure supplement 1. Characterization of *Meg3* isoforms. (A) Upper panel: Time-series expression of the PRC2 subunits (*Eed*, *Suz12*, *Jarid2*, and *Ezh2*) during ESC–MN differentiation. The levels of PRC2 complex progressively decreased during differentiation, whereas *Jarid2* is reactivated in Figure 3—figure supplement 1 continued on next page

Figure 3—figure supplement 1 continued

day 7 postmitotic MNs. Lower panel: The abundances of the known lncRNAs that interact with PRC2 in MNs, as revealed by RNA-seq. (B) RNA-seq analysis of ESC-MNs. Reads from ESCs, RA-induced nascent neural epithelium (NE at day 2), MN progenitors (pMN at day 4), postmitotic interneurons (IN at day 7), and postmitotic MNs (MN at day 7). Reads are normalized to the total number of mappable reads per sample. RNA-seq revealed that *Meg3^{v1}* (blue boxes) and *Meg3^{v5}* (pink boxes) are the most abundant *Meg3* isoforms in postmitotic MNs (GENCODE version M9). (C) Radar chart reveals that day 7 postmitotic MNs have the highest distribution of *Meg3^{v5}* during ESC-MN differentiation. (D) Histogram plot indicates that the *Meg3^{v1}* and *Meg3^{v5}* isoforms account for more than 99% of *Meg3* transcripts during ESC-MN differentiation. (E) Schematic diagram of RT-PCR primer locations within the *Meg3^{v1}* and *Meg3^{v5}* regions. Expression of *Meg3* according to different primer combinations for *Meg3* isoforms suggests that *Meg3^{v1}* and *Meg3^{v5}* are independent transcripts. *Gapdh* as a loading control. (F) Western blot shows that the loss of *Meg3* imprinted lncRNAs does not affect the protein abundance of Ezh2 and Jarid2 in ESC-MNs.

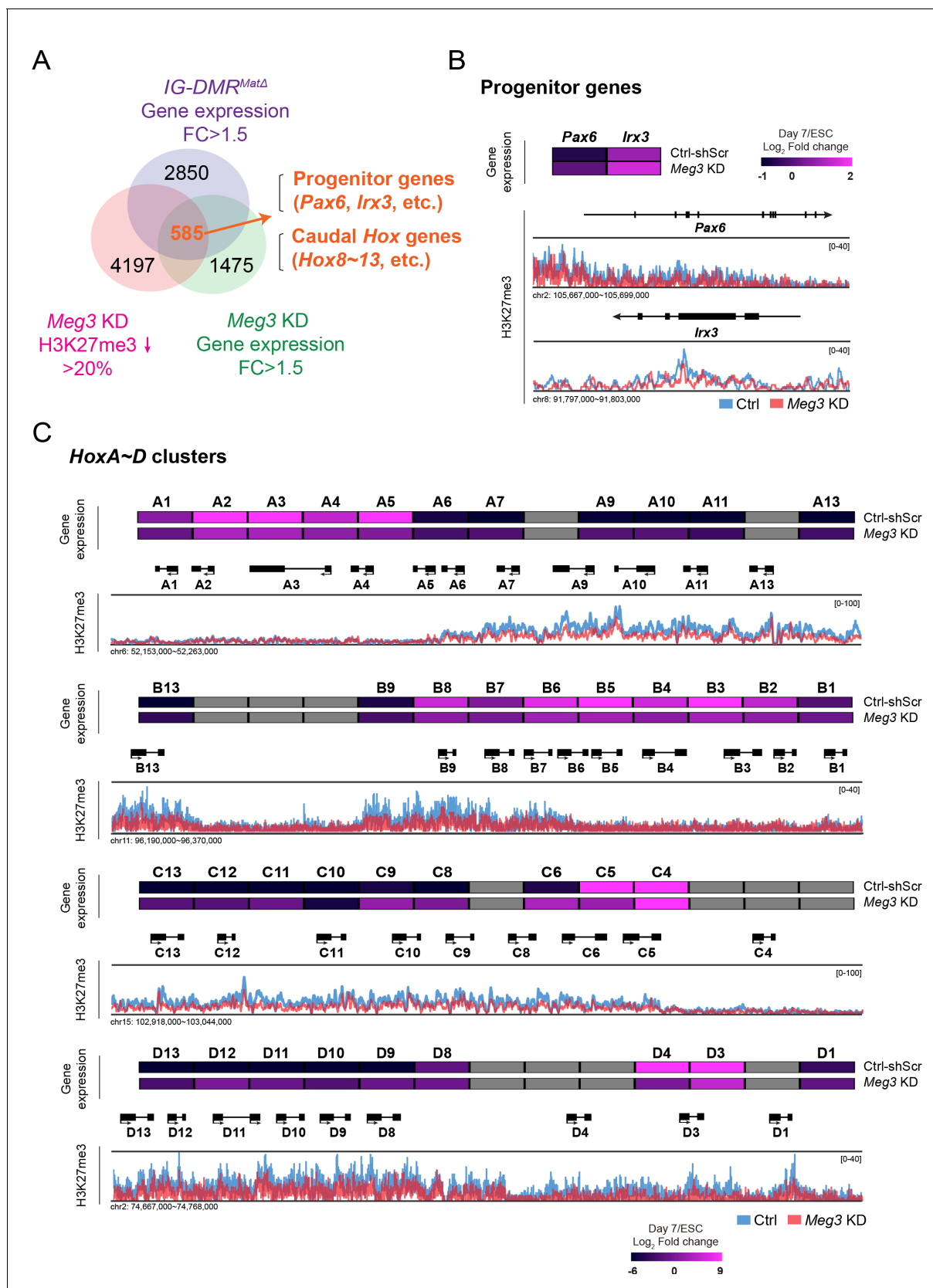


Figure 4. Loss of *Dlk1-Dio3* locus-derived lncRNAs in MNs leads to dysregulation of neural progenitor and caudal *Hox* genes. (A) Genome-wide profiling of H3K27me3 by ChIP-seq and gene expression by Agilent microarray in control, *IG-DMR^{matΔ}*, and *Meg3* KD ESC-MNs. Venn diagram shows

Figure 4 continued on next page

Figure 4 continued

the number of genes that are up-regulated in both *IG-DMR^{matA}* and *Meg3* KD MNs while also displaying the reduction of H3K27me3 epigenetic landscape. Loss of *Meg3* imprinted lncRNAs is related to the up-regulation of progenitor genes, as well as *Hox* genes. **(B and C)** Heatmaps illustrating the expression profiles of ESC-MNs in control scrambled and *Meg3* KD lines. The color indicates the log₂ fold-change in signal intensity between ESCs and ESC-MNs. Genes in light grey are not represented in the microarrays. Loss of *Meg3* imprinted lncRNAs results in ectopic expression of progenitor genes in **(B)**, and a majority of caudal *Hox* genes (*Hox8–13*) in **(C)**, with concomitant down-regulation of H3K27me3 levels.

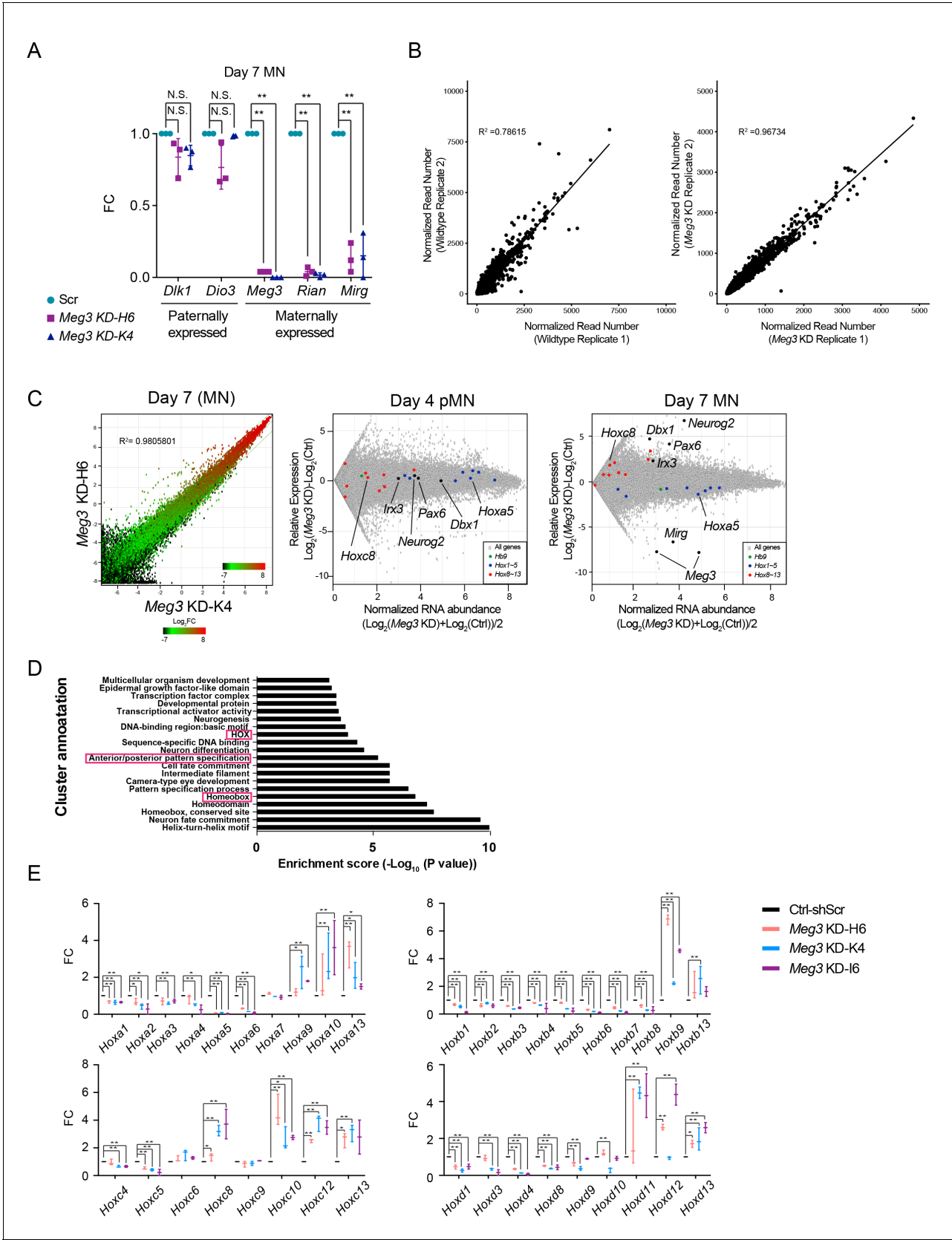


Figure 4—figure supplement 1. Characterization of *Meg3* KD ESCs. (A) Expression of paternally-expressed protein coding genes (*Dlk1* and *Dio3*) and maternally-expressed lncRNAs (*Meg3*, *Rian*, and *Mirg*) within the imprinted *Dlk1-Dio3* locus in ESC-MNs, as revealed by qPCR (FC: fold-change; N.S.: Figure 4—figure supplement 1 continued on next page

Figure 4—figure supplement 1 continued

not significant; error bars represent SD, $n = 3$ independent experiments; * p -value <0.05 , ** p -value <0.01 by Student's t -test). (B) The correlation plots and associated R^2 values are indicated by comparing H3K27me3 of MN samples from two independent controls and *Meg3* KD lines. (C) Left panel: The correlation plots and associated R^2 values indicate that the two *Meg3* KD lines infected by independent shRNAs are almost identical. Middle and right panels: MA plot of control versus *Meg3* KD pMNs (middle) and MNs (right). At the postmitotic stage (day 7), *Meg3* KD leads to up-regulation of the neural progenitor genes *Pax6*, *Dbx1*, *Neurog2*, *Irx3* and caudal *Hox* genes (*Hox8–13*), as well as down-regulation of rostral *Hox* genes (*Hox1–5*). Two biological replicate experiments were used to generate the data. The generic MN marker *Hb9* is unaffected, whereas *Meg3* and *Mirg* are the most down-regulated genes after *Meg3* KD. (D) Dysregulated genes are grouped by gene ontology (GO). (E) Loss of *Meg3* leads to ectopic expression of most caudal *Hox* genes (*Hox8–13*), with concomitant down-regulation of rostral *Hox* genes (*Hox1–5*), as verified by qPCR. A third shRNA (l6) was further assessed and *Hox* expression was normalized against *Gapdh* expression levels (FC: fold-change; error bars represent SD, $n = 3$; * p -value <0.05 , ** p -value <0.01 by Student's t -test).

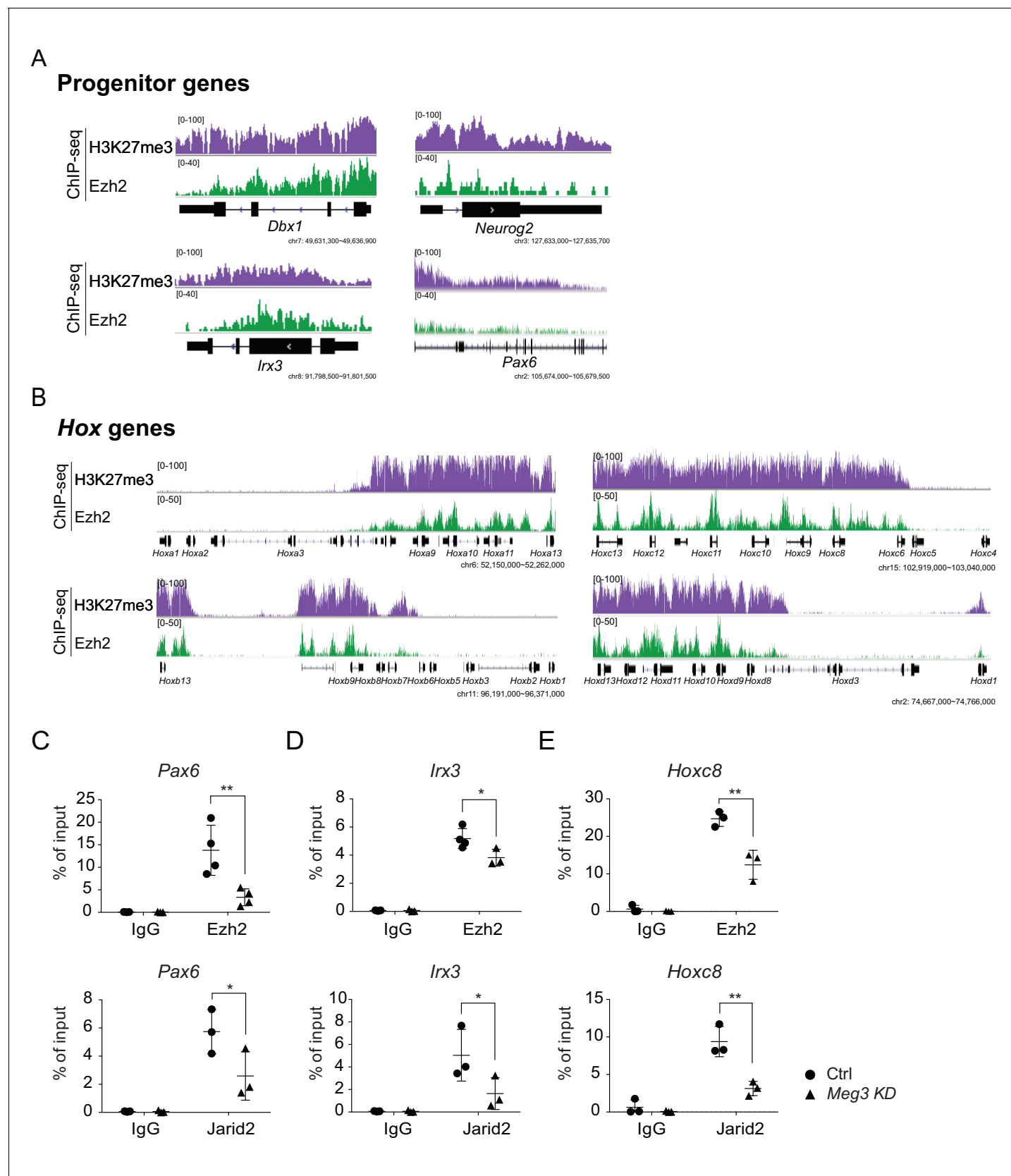


Figure 4—figure supplement 2. Ezh2 binding and the H3K27me3 landscape in ESC-MNs. (A and B) Concordant enrichments of Ezh2 and H3K27me3 in progenitor genes (A) and caudal *Hox* genes (B). (C–E) ChIP-qPCR verifies compromised H3K27me3 occupancy of Ezh2 and Jarid2 for the *Pax6*, *Irx3*, *Hoxc8*. Figure 4—figure supplement 2 continued on next page

Figure 4—figure supplement 2 continued

and *Hoxc8* loci upon *Meg3* KD. 1% input was used to normalize the retrieval efficiency (error bars represent SD, n = 3 independent experiments; * p-value<0.05, ** p-value<0.01 by Student's t-test).

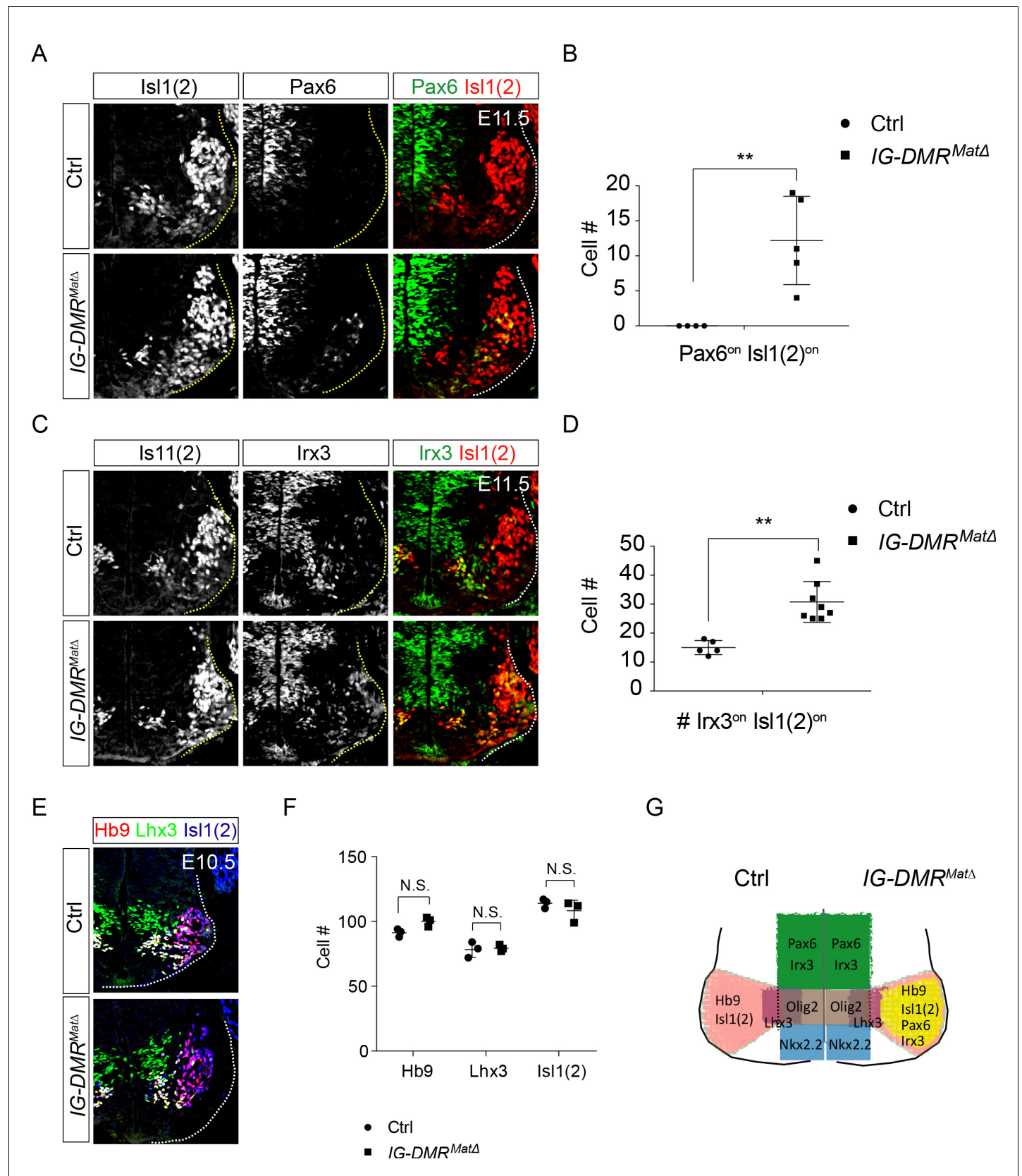


Figure 5. IG-DMR^{matΔ} mice ectopically turn on progenitor genes in postmitotic MNs. (A ~ D) IG-DMR^{matΔ} embryos display ectopic Pax6^{on} and Irx3^{on} cells in the postmitotic Isl1(2)^{on} MNs (partial penetrance for Pax6, n = 5/11 at E11.5; whereas Irx3 displays 100% penetrance, n = 8/8. Error bars

Figure 5 continued on next page

Figure 5 continued

represent SD, ** p-value<0.01 by Student's t-test). (E) Generation of generic MNs (Hb9^{on}, Lhx3^{on}, and Isl1/2^{on}) is not affected in spinal cords of *IG-DMR^{matΔ}* mice at E10.5. (F) Quantification of postmitotic MNs (number of positive cells per 15 μm brachial ventral-half sections) in wild type control and *IG-DMR^{matΔ}* embryos (error bars represent SD, n = 3 embryos at E10.5; N.S.: not significant by Student's t-test). (G) Summary of ectopic progenitor gene expression in postmitotic MNs of the *IG-DMR^{matΔ}* embryos.

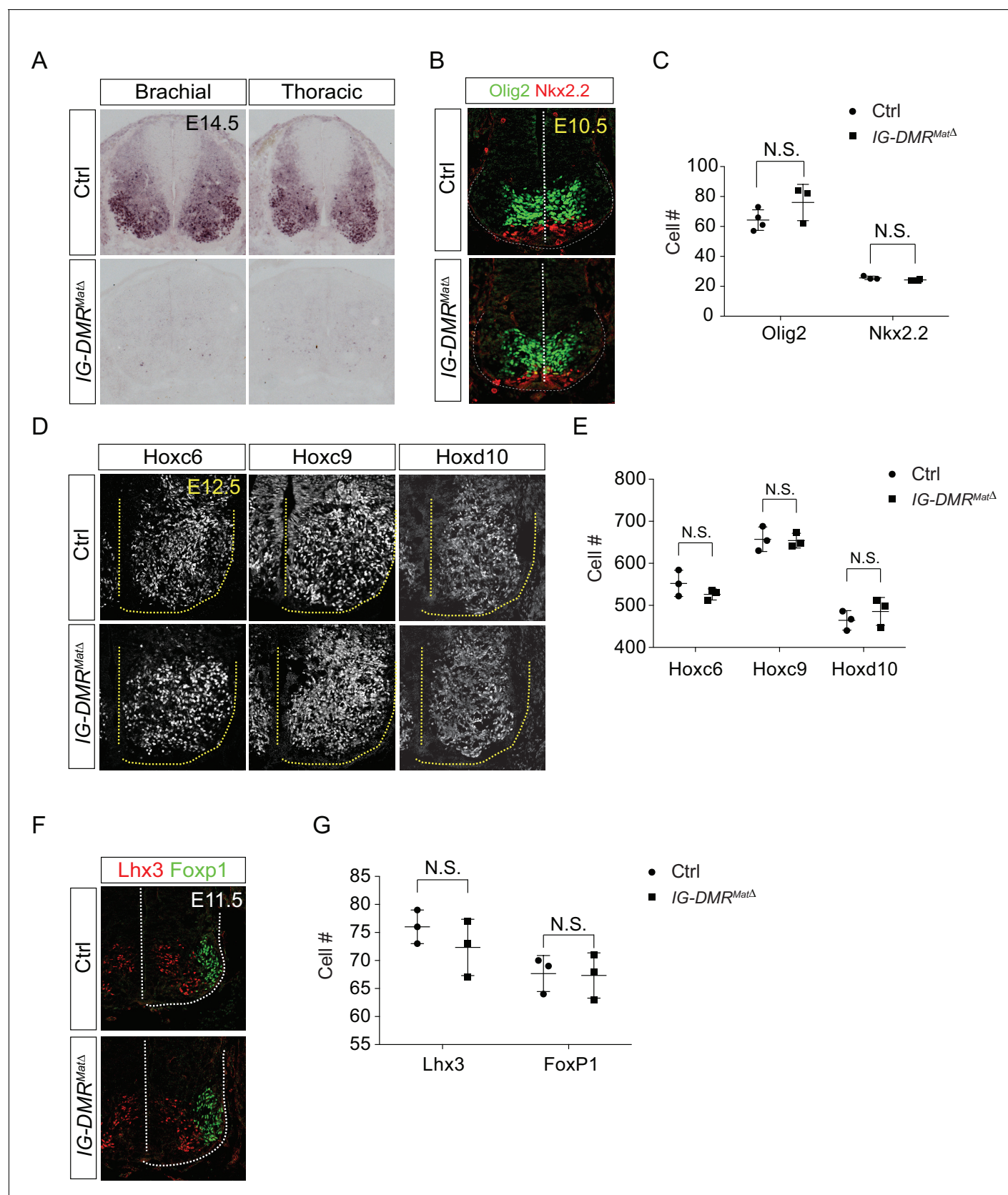


Figure 5—figure supplement 1. *IG-DMR^{matΔ}* mutant phenotype analysis. (A) *Meg3* is absent from the spinal cords of *IG-DMR^{matΔ}* embryos at E14.5, as revealed by in situ hybridization. (B and C) Immunostaining analysis of MN progenitors Nkx2.2 and Olig2 shows comparable numbers in wild type

Figure 5—figure supplement 1 continued on next page

Figure 5—figure supplement 1 continued

control and *IG-DMR^{matΔ}* spinal cord sections at E10.5. Quantification of MN progenitors (number of positive cells per 15 μm brachial spinal cord ventral-half sections) in wild type control and *IG-DMR^{matΔ}* embryos revealed no significant differences amongst different segments from the spinal cord (error bars represent SD, n = 3 embryos at E10.5; N.S.: not significant) (**D and E**) Immunostaining analysis of segmental MNs (Hoxc6^{on} at brachial, Hoxc9^{on} at thoracic, and Hoxd10^{on} at lumbar regions) shows comparable MN numbers for E12.5 wild type control and *IG-DMR^{matΔ}* spinal cord sections. Quantification of segmental MNs (number of positive cells per 15 μm brachial spinal cord ventral-half sections) in wild type control and *IG-DMR^{matΔ}* embryos revealed no significant differences amongst different segments from the spinal cord (error bars represent SD, n = 3 embryos at E12.5; N.S.: not significant). (**F and G**) Columnar axial MNs (Lhx3^{on}) and limb-innervating MNs (Foxp1^{on}) are unaffected in the *IG-DMR^{matΔ}* embryos. Quantification of columnar MNs (number of positive cells per 15 μm brachial spinal cord ventral-half sections) in wild type control and *IG-DMR^{matΔ}* embryos revealed no significant differences amongst different segments from the spinal cord (error bars represent SD, n = 3 embryos at E11.5; N.S.: not significant).

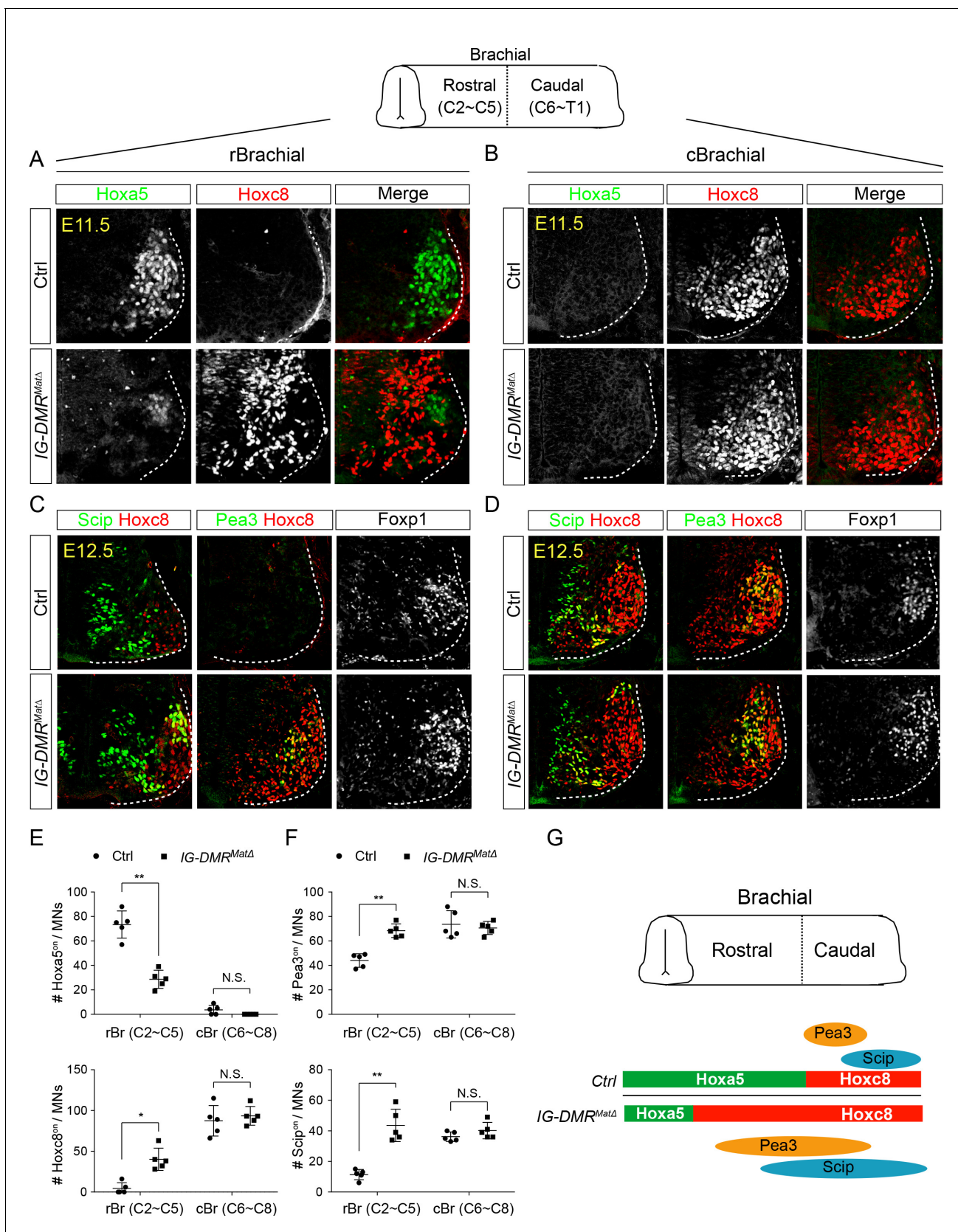


Figure 6. *IG-DMR^{matΔ}* mice manifest switched MN subtype identity. (A ~ D) Ectopic expansion of *Hoxc8* and downstream *Pea3*^{on} and *Scip*^{on} MN pools in the rostral brachial segment, with a concomitant decrease of *Hoxa5*^{on} MNs for E11.5~E12.5 *IG-DMR^{matΔ}* embryonic spinal cord sections. Expression Figure 6 continued on next page

Figure 6 continued

of Hoxc8 in the caudal brachial region remains unaffected (**B and D**). (**E and F**) Quantification of the numbers and distributions of Hoxa5^{on}, Hoxc8^{on}, Pea3^{on}, and Scip^{on} MNs in the control and *IG-DMR^{matΔ}* mice from serial sections along the rostrocaudal axis (N.S.: not significant; error bars represent SD, n = 5; * p-value<0.05, ** p-value<0.01 by Student's *t*-test). (**G**) Summary of the motor neuron phenotype in the *IG-DMR^{matΔ}* embryos.

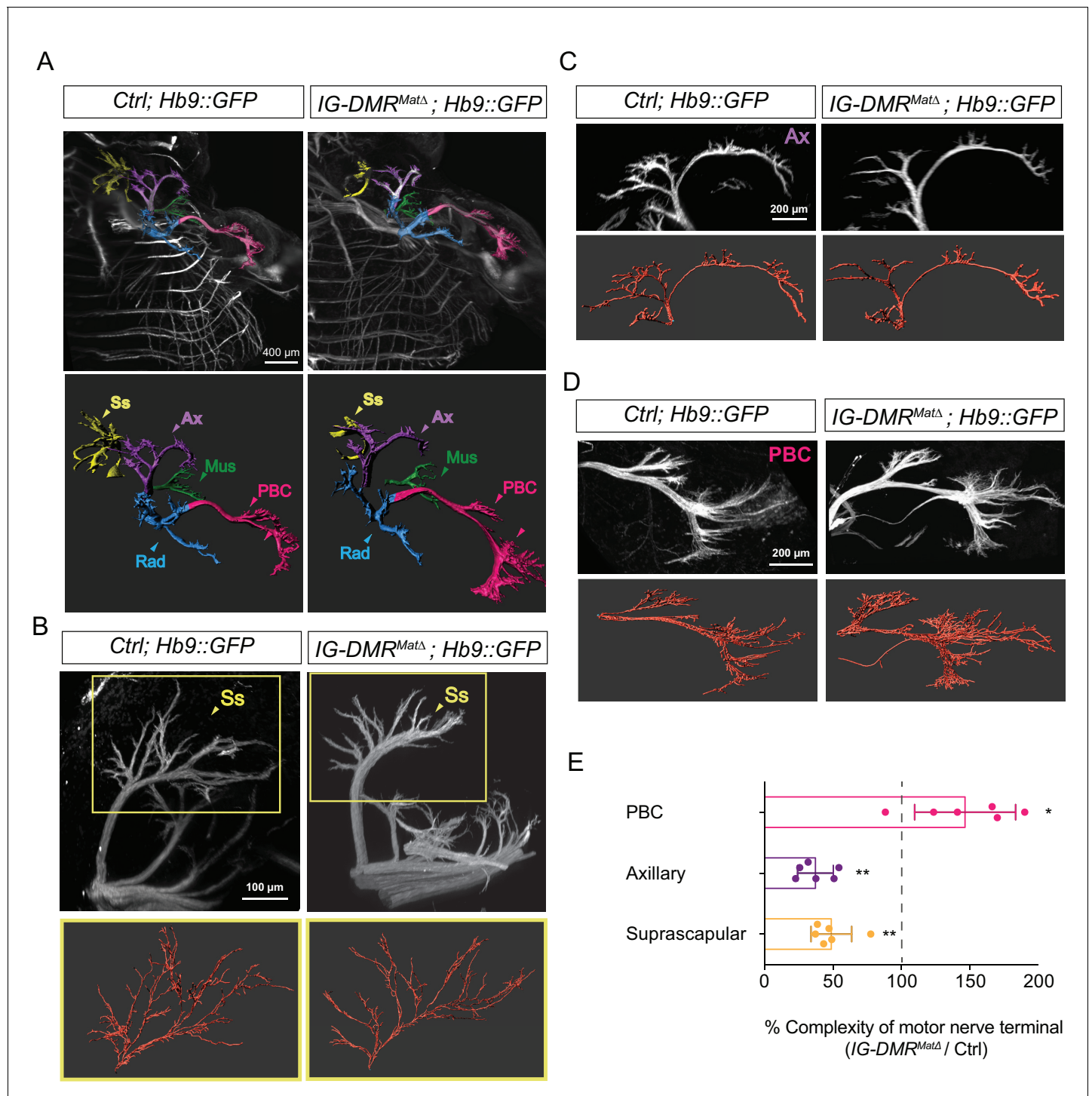


Figure 7. Motor axon innervation defects in the IG-DMR^{matΔ} embryos. (A) Panoramic views from different angles of control and IG-DMR^{matΔ}; Hb9::GFP embryos at E13.5 using light sheet microscopy (Upper panel). Details of each viewing angle are illustrated in **Videos 1** and **2**. Reconstruction of motor nerve positions by Imaris (see Materials and methods for details) is illustrated in the lower panel. Suprascapular nerve (Ss, yellow); axillary nerve (Ax, purple); musculocutaneous nerve (Mus, green); radial nerve (Rad, blue); posterior brachial cutaneous nerve (PBC, pink). (B ~ D) Higher magnification of MN innervations in the forelimbs of E13.5 control and IG-DMR^{matΔ}; Hb9::GFP mice. Mutant mice display defects in Ss and Ax axonal branching, concomitant with more PBC axonal branching. Semi-automatic highlighting of the axonal branching and nerve trajectories is used and quantified by Imaris. (E) Quantification of the axonal branching and nerve trajectories for E13.5 control and IG-DMR^{matΔ}; Hb9::GFP mice by Imaris (see Materials and methods for details) (n = 6, p < 0.01, Mann-Whitney U test).

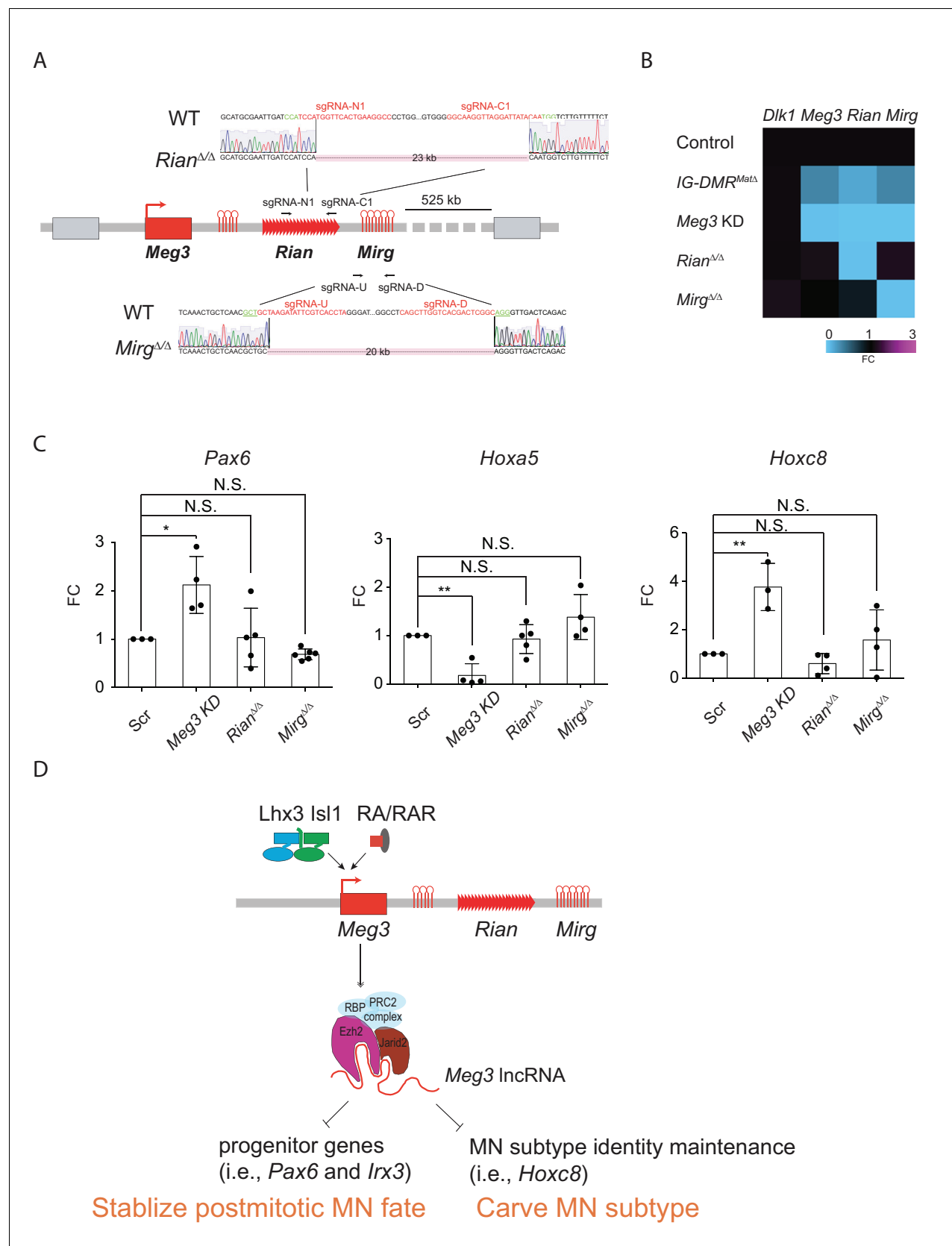


Figure 8. Dissection of individual roles of lncRNAs in the *Meg3-Rian-Mirg* locus in ESC-MNs. (A) Illustration of the sgRNAs target sites and sequences for the sgRNA:Cas9-mediated *Rian* and *Mirg* deletions respectively. Deleted sequences shown in *Rian*^{ΔΔ} and *Mirg*^{ΔΔ} ESC lines. The PAM sites are

Figure 8 continued on next page

Figure 8 continued

displayed in green; the sgRNA target sequences are reflected in red. (B) Heatmaps representing the abundances of the paternal gene (*Dlk1*) and maternal lncRNAs (*Meg3*, *Rian*, and *Mirg*) in control, *Meg3* KD, and KO (*IG-DMR^{matΔ}*, *Rian^{Δ/Δ}*, and *Mirg^{Δ/Δ}*) ESCs respectively. (C) Rostral *Hox* gene *Hoxa5* is significantly down-regulated in the *Meg3* KD line, whereas the expression of *Hoxa5* is comparable between *Rian^{Δ/Δ}* and *Mirg^{Δ/Δ}* when compared to the controls. Conversely, the expressions of progenitor gene *Pax6*, as well as caudal *Hox* gene *Hoxc8*, are significantly up-regulated in the *Meg3* KD line, while their expressions are restored between *Rian^{Δ/Δ}* and *Mirg^{Δ/Δ}* when compared to the controls. (FC: fold-change; error bars represent SD, n = 3–5, * p-value<0.05, ** p-value<0.01 by Student's t-test). (D) Summary of the functions of lncRNAs from the imprinted *Dlk1-Dio3* locus in ESC–MNs. *Meg3* and other lncRNAs from the *Dlk1-Dio3* locus are directly activated by MN-TFs (i.e., *Lhx3* and *Isl1*) and RAR, leading to enrichment of *Meg3* in the rostral segment of postmitotic MNs. One major function of *Meg3* and other lncRNAs from the *Dlk1-Dio3* locus is to stimulate *Ezh2/Jarid2* interactions. Loss of these lncRNAs compromises the H3K27me3 epigenetic landscape and leads to aberrant expressions of progenitor and caudal *Hox* genes in postmitotic MNs. Our model illustrates that the lncRNAs of the imprinted *Dlk1-Dio3* locus (*Meg3* particularly) play a critical role in maintaining postmitotic MN cell fate by repressing progenitor genes, and that they shape MN subtype identity by regulating *Hox* genes.